The Astrophysical Journal, 836:79 (6pp), 2017 February 10 https://doi.org/10.3847/1538-4357/836/1/79


# The Synthesis of $^{44}$Ti and $^{56}$Ni in Massive Stars

Alessandro Chieffi[1,2] and Marco Limongi[3,4]
[1] Istituto Nazionale di Astrofisica—Istituto di Astrofisica e Planetologia Spaziali, Via Fosso del Cavaliere 100, I-00133, Roma, Italy; alessandro.chieffi@inaf.it
[2] Centre for Stellar & Planetary Astrophysics, School of Mathematical Sciences, P.O. Box, 28M, Monash University, Victoria 3800, Australia
[3] Istituto Nazionale di Astrofisica—Osservatorio Astronomico di Roma, Via Frascati 33, I-00040, Monteporzio Catone, Italy; marco.limongi@oa-roma.inaf.it
[4] Kavli Institute for the Physics and Mathematics of the Universe, Todai Institutes for Advanced Study, The University of Tokyo, Kashiwa 277-8583 (Kavli IPMU, WPI), Japan
*Received 2016 October 27; revised 2017 January 9; accepted 2017 January 9; published 2017 February 9*

## Abstract

We discuss the influence of rotation on the combined synthesis of $^{44}$Ti and $^{56}$Ni in massive stars. While $^{56}$Ni is significantly produced by both complete and incomplete explosive Si burning, $^{44}$Ti is mainly produced by complete explosive Si burning, with a minor contribution (in standard non-rotating models) from incomplete explosive Si burning and O burning (both explosive and hydrostatic). We find that, in most cases, the thickness of the region exposed to incomplete explosive Si burning increases in rotating models (initial velocity, $v_{\rm ini} = 300\,{\rm km\,s^{-1}}$) and since $^{56}$Ni is significantly produced in this zone, the fraction of mass coming from the complete explosive Si burning zone necessary to get the required amount of $^{56}$Ni reduces. Therefore the amount of $^{44}$Ti ejected for a given fixed amount of $^{56}$Ni decreases in rotating models. However, some rotating models at [Fe/H] $= -1$ develop a very extended O convective shell in which a consistent amount of $^{44}$Ti is formed, preserved, and ejected in the interstellar medium. Hence a better modeling of the thermal instabilities (convection) in the advanced burning phases together with a critical analysis of the cross sections of the nuclear reactions operating in O burning are relevant for the understanding of the synthesis of $^{44}$Ti.

*Key words:* stars: abundances – stars: evolution – stars: interiors – stars: massive – stars: rotation – supernovae: general

## 1. Introduction

Neutral $^{44}$Ti is an isotope unstable to $e^-$ capture with a half-life of 58.9 ± 0.3 yr (Ahmad et al. 2006). It decays to $^{44}$Sc first by emitting a $\gamma$ of 1157 keV and to $^{44}$Ca later by emitting two additional $\gamma$ rays of 67.9 and 78.4 keV. Since the 1960s (Bodansky et al. 1968; Woosley et al. 1973), it has been recognized that may be produced in the very deep regions of a massive star during the explosion if the regions are shocked to very high temperatures (greater than 5 GK or so) to reach Nuclear Statistical Equilibrium but then cooled (expanded) rapidly enough that a large amount of free $\alpha$ particles is left ($\alpha$-rich freeze-out). In this case, there is a temporal "window" of the order of 200–300 ms in which the local temperature $T$ and density $\rho$ of these expanding layers are sufficiently high for the nuclear reactions to activate in the presence of fuel ($\alpha$ particles in this case). Within this scenario, the synthesis of $^{44}$Ti has always been explored by parametric studies of the properties of the $\alpha$-rich freeze-out as a function of various parameters, mainly $T$, $\rho$, electron mole number Ye, and the relevant nuclear reaction rates (The et al. 1998, 2006; Magkotsios et al. 2010). An important constraint that a model must satisfy in order to provide a meaningful prediction of $^{44}$Ti is avoidance of overproduction of $^{56}$Ni, another unstable nucleus synthesized in complete and incomplete explosive Si burning.

From an observational point of view, the quest for a signal from the decay of $^{44}$Ti started as soon as the first X- and $\gamma$-ray detectors where launched in the 1980s (Mahoney et al. 1992; Iyudin et al. 1994; Leising & Share 1994; Dupraz et al. 1997). After more than 30 years of data taken by several satellites, at present we have only two clear evidences of the presence of live $^{44}$Ti: a first one from the supernova remnant Cas A and a second one from the SN 1987A in the Large Magellanic Cloud.

The signal from Cas A is well secured, the latest available data (the 78.36 and 1157 keV lines detected by *INTEGRAL* give $(1.37 \pm 0.19) \times 10^{-4}\ M_\odot$ (Siegert et al. 2015), the 67.86 and 78.36 keV lines detected by *NuSTAR* give $(1.25 \pm 0.3) \times 10^{-4}\ M_\odot$ (Grefenstette et al. 2014)) converging toward an amount of $^{44}$Ti of the order of $(1 \div 1.3) \times 10^{-4}\ M_\odot$. Another recent finding (Grefenstette et al. 2014) concerns the strong asymmetries in the spatial distribution of $^{44}$Ti around this supernova remnant together with the fact that it appears uncorrelated with the Fe X-ray emission (*CHANDRA* data). Though these data are fundamental and necessary to constrain the explosion properties of this star, a reliable estimate of the amount of $^{56}$Ni ejected is unfortunately missing. According to the analysis of the proper motion of the ejecta, this supernova should have exploded in 1671 but the appearance of a "new" star was not reported at that time (with the possible exception of Flamsted in 1680). Since the luminosity of a supernova is directly connected to the amount of $^{56}$Ni ejected during the explosion (because the light curve is powered by the decay of $^{56}$Ni first and $^{56}$Co later) and given its proximity (3.4 kpc), the lack of detection puts strong limits on the maximum amount of $^{56}$Ni ejected. The situation is even more complex because the explosion could have been obscured by the presence of a large amount of circumstellar matter. A recent analysis of the reddening in the direction of this supernova remnant (Eriksen et al. 2009) shows that the amount of $^{56}$Ni could have been as large as 0.15 $M_\odot$ and still be not visible from the Earth. At present, we can only state that we do not know how much $^{56}$Ni was ejected in this event.

As far as SN 1987A is concerned, we have more stringent data because we know both the amount of $^{56}$Ni ejected during the explosion ($\simeq$0.075 $M_\odot$; Catchpole et al. 1988; Seitenzahl et al. 2014) and the amount of $^{44}$Ti present in the ejecta. In fact, *NuSTAR* detected both the 67.86 and 78.36 keV lines and

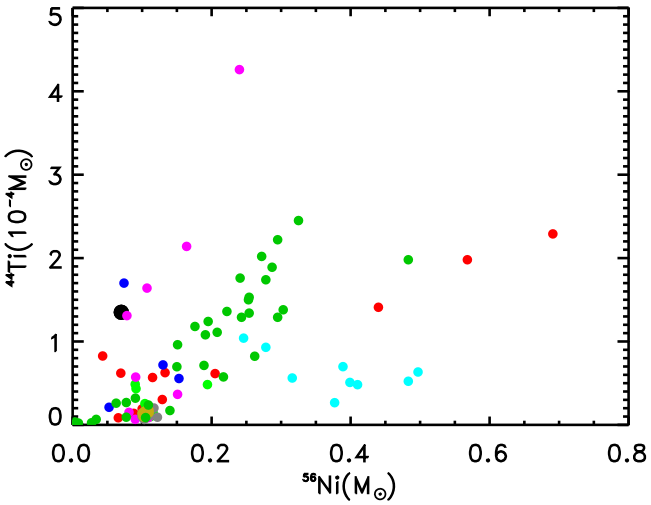


**Figure 1.** Ejected amount of $^{44}$Ti vs. $^{56}$Ni for different sets of models; red (Woosley & Weaver 1995), blue (Thielemann et al. 1996), magenta (Maeda & Nomoto 2003), cyan (Magkotsios et al. 2010), light green (Rauscher et al. 2002), dark green (Limongi & Chieffi 2003), brown and gray (Chieffi & Limongi 2013) non-rotating and rotating models, respectively. The black dot represents the position of the SN 1987A.

derived a $^{44}$Ti abundance of $1.5 \pm 0.3 \times 10^{-4}\,M_\odot$ (Boggs et al. 2015) while *INTEGRAL* was able to measure only a combined flux of the 67.86 and 78.36 keV lines and derived a $^{44}$Ti abundance of $3.1 \pm 0.8 \times 10^{-4}\,M_\odot$ (Grebenev et al. 2012). A recent analysis of the UVOIR light curve of 1987A by Seitenzahl et al. (2014) reported an amount of $^{44}$Ti of the order of $0.55 \pm 0.17 \times 10^{-4}\,M_\odot$ necessary to power the light curve at late times. Given the uncertainties (which are larger than the formal error bars), we feel confident in saying that 1987A very probably ejected something between 1 and $2 \times 10^{-4}\,M_\odot$ of $^{44}$Ti. The somewhat poorer knowledge of the amount of $^{44}$Ti ejected in this explosion is largely counterbalanced by a very good knowledge of the amount of $^{56}$Ni ejected.

As far as we know, the available evolutionary models fail to predict the right amount of $^{44}$Ti (corresponding to an amount of $^{56}\mathrm{Ni} \simeq 0.07\,M_\odot$) by a factor of the order of three or more. Figure 1 shows the amount of $^{44}$Ti and $^{56}$Ni ejected by a number of models (see the figure caption). The big black dot marks the values corresponding to the supernova remnant 1987A. It is evident that no models are compatible with the observed values. The only one that fits 1987A comes from an aspherical explosion of a pure He core of $8\,M_\odot$ that should represent the He core of a $25\,M_\odot$ (Maeda & Nomoto 2003). The interpretation of Cas A is more difficult, but it is clear that the observed amount of $^{44}$Ti can be reconciled with the existing models only if the exploding star ejected at least $0.15\,M_\odot$ of $^{56}$Ni.

After the publication of a first set of rotating solar metallicity models (Chieffi & Limongi 2013), we have now completed the computation of a much larger set of models that extends in mass between 13 and $120\,M_\odot$, in metallicity between $[\mathrm{Fe/H}] = 0$ and $-3$, and covers three initial rotational velocities (0, 150, and 300 km s$^{-1}$). All the details of these new models will be published in a companion paper (M. Limongi & A. Chieffi 2017, in preparation). Here we have extracted the yields of $^{44}$Ti and $^{56}$Ni from that large set because we think they are worth a separate discussion. This paper is organized as follows: the basic properties of the models are reported in the next section while an analysis of the results is presented in Section 3.

## 2. The Models

The results presented in this paper are based on a grid of models having initial masses 13, 15, 20, 25, 30, 40, 60, 80, and $120\,M_\odot$, initial metallicities $[\mathrm{Fe/H}] = 0, -1, -2, -3$, and initial equatorial velocities $v = 0$, 150, 300 km s$^{-1}$. The adopted solar chemical composition is the one identified by Asplund et al. (2009). At lower metallicities, following Cayrel et al. (2004) and Spite et al. (2005), we assume that a few elemental species are enhanced with respect to the scaled solar composition. In particular, we adopt $[\mathrm{C/Fe}] = 0.18$, $[\mathrm{O/Fe}] = 0.47$, $[\mathrm{Mg/Fe}] = 0.27$, $[\mathrm{Si/Fe}] = 0.37$, $[\mathrm{S/Fe}] = 0.35$, $[\mathrm{Ar/Fe}] = 0.35$, $[\mathrm{Ca/Fe}] = 0.33$, and $[\mathrm{Ti/Fe}] = 0.23$ at all metallicities lower than solar. The initial He abundances are $Y = 0.265$ ($[\mathrm{Fe/H}] = 0$), 0.25 ($[\mathrm{Fe/H}] = -1$), and 0.24 ($[\mathrm{Fe/H}] < -1$).

All models were followed from the pre Main Sequence phase up to the onset of the final collapse by means of the latest version of our code, the FRANEC. The main features of this code, as well as all the input physics and assumptions, have already been extensively discussed in Chieffi & Limongi (2013) and will not be repeated here. The only improvements with respect to the version described in Chieffi & Limongi (2013) are (1) a better treatment of the angular momentum transport in the envelope of the star, (2) the inclusion of a proper mass loss that activates when the star approaches the Eddington limit, (3) a refined computation of the angular momentum loss due to the stellar wind, and (4) a more extended nuclear network. Though the evolutionary properties of all these stars will be discussed in M. Limongi & A. Chieffi (2017, in preparation), it is worth mentioning here that one of the key (and direct) effects of rotation on the advanced burning phases is a systematic reduction of the $^{12}\mathrm{C}/^{16}\mathrm{O}$ ratio as a consequence of the continuous ingestion of fresh He during the latest phases of the central He burning where most of the conversion of $^{12}$C to $^{16}$O occurs. This is relevant in the present context because, the lower the concentration of $^{12}$C, the faster the C burning shell advances in mass leaving room for the possible formation of an extended O convective shell (see below).

The explosion of the mantle of each stellar model was followed by means of a hydrodynamic code we developed that solves the fully compressible reactive hydrodynamic equations using the Piecewise Parabolic Method of Colella & Woodward (1984) in Lagrangean form. Since the explosions cannot be computed yet on the basis of first principles, we still have to rely on a parametric approach in which some arbitrary amount of energy is injected in the deep interior of the models. More specifically, each explosion is started by means of a kinetic bomb, i.e., by instantaneously imparting an initial velocity $v_0$ to a mass coordinate of $\sim 1\,M_\odot$, i.e., well within the iron core (Limongi & Chieffi 2006), and followed for $10^8$ s, well after the expanding envelope has become homologous. Each (arbitrary) initial velocity $v_0$ will correspond to a specific mass cut and abundances of all the nuclear species synthesized in the deepest regions of the star. The explosions presented in Table 1 were computed by requiring that each model ejects of $0.07\,M_\odot$ of $^{56}$Ni.

**Table 1**
Abundances of $^{44}$Ti and $^{56}$Ni

| $M_{ini}$ ($M_\odot$) (1) | $M_{cut}$ ($M_\odot$) (2) | $M$(Siix) ($M_\odot$) (3) | $M$(Ox) ($M_\odot$) (4) | $^{44}$Ti $M_{cut}$ ($M_\odot$) (5) | $^{44}$Ti Siix ($M_\odot$) (6) | $^{44}$Ti Ox ($M_\odot$) (7) | $^{56}$Ni $M_{cut}$ ($M_\odot$) (8) | $^{56}$Ni Siix ($M_\odot$) (9) | $^{56}$Ni Ox ($M_\odot$) (10) | $^{44}$Ti $M_{cut}$ (%) (11) | $^{44}$Ti Siix (%) (12) | $^{44}$Ti Ox (%) (13) | $^{56}$Ni $M_{cut}$ (%) (14) | $^{56}$Ni Siix (%) (15) | $^{56}$Ni Ox (%) (16) |
|---|---|---|---|---|---|---|---|---|---|---|---|---|---|---|---|
| [Fe/H] = 0 $v$ = 0 km s$^{-1}$ | | | | | | | | | | | | | | | |
| 13 | 1.52 | 1.59 | 1.65 | 2.6(−05) | 2.2(−06) | 6.6(−07) | 7.0(−02) | 1.2(−02) | 4.4(−05) | 91.7 | 5.7 | 2.6 | 82.6 | 17.3 | 0.1 |
| 15 | 1.63 | 1.68 | 1.80 | 1.3(−05) | 3.7(−06) | 9.9(−07) | 7.0(−02) | 2.5(−02) | 8.2(−06) | 71.4 | 21.0 | 7.6 | 63.9 | 36.1 | 0.0 |
| 20 | 1.62 | 1.67 | 1.79 | 1.5(−05) | 4.0(−06) | 1.5(−06) | 7.0(−02) | 2.9(−02) | 2.7(−04) | 73.1 | 16.5 | 10.4 | 58.0 | 41.6 | 0.4 |
| 25 | 1.87 | 1.91 | 2.06 | 8.9(−06) | 5.3(−06) | 1.9(−06) | 7.0(−02) | 4.4(−02) | 6.3(−05) | 39.9 | 38.5 | 21.5 | 37.8 | 62.1 | 0.1 |
| 30 | 2.66 | 2.66 | 3.08 | 1.3(−05) | 1.3(−05) | 3.2(−06) | 7.0(−02) | 7.0(−02) | 1.9(−05) | 0.0 | 75.7 | 24.3 | 0.0 | 100.0 | 0.0 |
| 40 | 2.66 | 2.66 | 2.94 | 1.3(−05) | 1.3(−05) | 6.9(−06) | 7.0(−02) | 7.0(−02) | 1.4(−03) | 0.0 | 48.2 | 51.8 | 0.0 | 98.0 | 2.0 |
| 60 | 3.23 | 3.23 | 3.72 | 1.9(−05) | 1.9(−05) | 8.6(−06) | 7.0(−02) | 7.0(−02) | 1.1(−03) | 0.0 | 54.4 | 45.6 | 0.0 | 98.4 | 1.6 |
| 80 | 4.25 | 4.25 | 4.92 | 3.0(−05) | 3.0(−05) | 1.6(−05) | 7.0(−02) | 7.0(−02) | 1.4(−03) | 0.0 | 47.6 | 52.4 | 0.0 | 98.0 | 2.0 |
| 120 | 4.73 | 4.73 | 5.42 | 3.1(−05) | 3.1(−05) | 2.0(−05) | 7.0(−02) | 7.0(−02) | 3.9(−03) | 0.0 | 36.1 | 63.9 | 0.0 | 94.5 | 5.5 |
| [Fe/H] = 0 $v$ = 300 km s$^{-1}$ | | | | | | | | | | | | | | | |
| 13 | 2.02 | 2.05 | 2.27 | 2.6(−05) | 2.4(−05) | 1.8(−05) | 7.0(−02) | 4.2(−02) | 4.8(−04) | 8.3 | 22.0 | 69.6 | 39.4 | 59.9 | 0.7 |
| 15 | 2.30 | 2.35 | 2.77 | 6.0(−06) | 5.9(−06) | 2.1(−06) | 7.0(−02) | 4.4(−02) | 1.6(−06) | 1.7 | 63.6 | 34.7 | 37.3 | 62.7 | 0.0 |
| 20 | 2.72 | 2.72 | 3.17 | 1.3(−05) | 1.3(−05) | 3.9(−06) | 7.0(−02) | 7.0(−02) | 1.3(−05) | 0.0 | 70.5 | 29.5 | 0.0 | 100.0 | 0.0 |
| 25 | 2.49 | 2.49 | 2.86 | 1.4(−05) | 1.4(−05) | 4.9(−06) | 7.0(−02) | 7.0(−02) | 4.1(−04) | 0.0 | 63.8 | 36.2 | 0.0 | 99.4 | 0.6 |
| 30 | 2.36 | 2.36 | 2.63 | 1.3(−05) | 1.3(−05) | 6.3(−06) | 7.0(−02) | 7.0(−02) | 1.0(−03) | 0.0 | 51.3 | 48.7 | 0.0 | 98.5 | 1.5 |
| 40 | 2.95 | 2.95 | 3.27 | 1.7(−05) | 1.7(−05) | 1.1(−05) | 7.0(−02) | 7.0(−02) | 2.7(−03) | 0.0 | 38.9 | 61.1 | 0.0 | 96.1 | 3.9 |
| 60 | 3.30 | 3.30 | 3.74 | 1.9(−05) | 1.9(−05) | 1.0(−05) | 7.0(−02) | 7.0(−02) | 3.0(−03) | 0.0 | 44.6 | 55.4 | 0.0 | 95.7 | 4.3 |
| 80 | 3.47 | 3.47 | 3.95 | 2.1(−05) | 2.1(−05) | 1.2(−05) | 7.0(−02) | 7.0(−02) | 3.2(−03) | 0.0 | 41.6 | 58.4 | 0.0 | 95.5 | 4.5 |
| 120 | 3.49 | 3.49 | 4.11 | 2.1(−05) | 2.1(−05) | 6.4(−06) | 7.0(−02) | 7.0(−02) | 1.1(−05) | 0.0 | 68.8 | 31.2 | 0.0 | 100.0 | 0.0 |
| [Fe/H] = −1 $v$ = 0 km s$^{-1}$ | | | | | | | | | | | | | | | |
| 13 | 1.53 | 1.60 | 1.66 | 2.3(−05) | 2.6(−06) | 8.1(−07) | 7.0(−02) | 1.5(−02) | 5.1(−05) | 88.7 | 7.8 | 3.5 | 78.2 | 21.7 | 0.1 |
| 15 | 1.69 | 1.72 | 1.91 | 9.1(−06) | 6.3(−06) | 1.8(−06) | 7.0(−02) | 4.4(−02) | 1.3(−05) | 31.3 | 49.5 | 19.2 | 36.8 | 63.2 | 0.0 |
| 20 | 1.74 | 1.78 | 1.92 | 9.9(−06) | 4.3(−06) | 1.1(−06) | 7.0(−02) | 3.5(−02) | 4.4(−06) | 56.9 | 31.9 | 11.2 | 50.3 | 49.7 | 0.0 |
| 25 | 2.48 | 2.48 | 2.84 | 1.3(−05) | 1.3(−05) | 3.4(−06) | 7.0(−02) | 7.0(−02) | 8.0(−05) | 0.0 | 74.2 | 25.8 | 0.0 | 99.9 | 0.1 |
| 30 | 2.52 | 2.52 | 2.91 | 1.4(−05) | 1.4(−05) | 3.2(−06) | 7.0(−02) | 7.0(−02) | 3.1(−05) | 0.0 | 77.4 | 22.6 | 0.0 | 100.0 | 0.0 |
| 40 | 2.65 | 2.65 | 2.97 | 1.6(−05) | 1.6(−05) | 6.0(−06) | 7.0(−02) | 7.0(−02) | 4.5(−04) | 0.0 | 63.7 | 36.3 | 0.0 | 99.4 | 0.6 |
| 60 | 4.48 | 4.48 | 5.10 | 3.9(−05) | 3.9(−05) | 1.8(−05) | 7.0(−02) | 7.0(−02) | 9.0(−04) | 0.0 | 53.6 | 46.4 | 0.0 | 98.7 | 1.3 |
| 80 | 6.96 | 6.96 | 7.70 | 5.3(−05) | 5.3(−05) | 2.5(−05) | 7.0(−02) | 7.0(−02) | 7.1(−04) | 0.0 | 52.5 | 47.5 | 0.0 | 99.0 | 1.0 |
| 120 | 5.73 | 5.73 | 6.37 | 6.0(−05) | 6.0(−05) | 4.6(−05) | 7.0(−02) | 7.0(−02) | 9.1(−03) | 0.0 | 23.5 | 76.5 | 0.0 | 87.0 | 13.0 |
| [Fe/H] = −1 $v$ = 300 km s$^{-1}$ | | | | | | | | | | | | | | | |
| 13 | 2.10 | 2.13 | 2.36 | 3.9(−05) | 3.4(−05) | 2.9(−05) | 7.0(−02) | 5.0(−02) | 6.2(−05) | 12.5 | 12.8 | 74.7 | 28.3 | 71.6 | 0.1 |
| 15 | 2.23 | 2.27 | 2.47 | 4.6(−05) | 4.5(−05) | 4.1(−05) | 7.0(−02) | 3.8(−02) | 1.1(−03) | 2.1 | 8.3 | 89.6 | 45.3 | 53.1 | 1.5 |
| 20 | 2.62 | 2.62 | 2.98 | 1.3(−05) | 1.3(−05) | 5.7(−06) | 7.0(−02) | 7.0(−02) | 1.5(−03) | 0.0 | 55.0 | 45.0 | 0.0 | 97.9 | 2.1 |
| 25 | 2.89 | 2.89 | 3.26 | 2.0(−05) | 2.0(−05) | 8.8(−06) | 7.0(−02) | 7.0(−02) | 8.6(−04) | 0.0 | 54.9 | 45.1 | 0.0 | 98.8 | 1.2 |
| 30 | 3.70 | 3.70 | 4.19 | 2.6(−05) | 2.6(−05) | 1.2(−05) | 7.0(−02) | 7.0(−02) | 8.6(−04) | 0.0 | 55.3 | 44.7 | 0.0 | 98.8 | 1.2 |
| 40 | 4.28 | 4.28 | 4.84 | 3.1(−05) | 3.1(−05) | 1.6(−05) | 7.0(−02) | 7.0(−02) | 1.2(−03) | 0.0 | 49.3 | 50.7 | 0.0 | 98.3 | 1.7 |
| 60 | 5.05 | 5.05 | 5.63 | 3.8(−05) | 3.8(−05) | 2.4(−05) | 7.0(−02) | 7.0(−02) | 4.3(−03) | 0.0 | 36.5 | 63.5 | 0.0 | 93.9 | 6.1 |
| 80 | 5.76 | 5.76 | 6.28 | 4.4(−05) | 4.4(−05) | 3.3(−05) | 7.0(−02) | 7.0(−02) | 8.4(−03) | 0.0 | 25.4 | 74.6 | 0.0 | 88.0 | 12.0 |
| 120 | 8.01 | 8.01 | 8.61 | 5.8(−05) | 5.8(−05) | 4.5(−05) | 7.0(−02) | 7.0(−02) | 8.6(−03) | 0.0 | 23.6 | 76.4 | 0.0 | 87.7 | 12.3 |

**Note.** The notation $(-y)$ stands for $10^{-y}$.

## 3. Discussion

The profiles of the abundances (in mass fraction) of O, Si, $\alpha$, $^{44}$Ti, and $^{56}$Ni after the passage of the shock wave, within the innermost layers of a non-rotating 20 $M_\odot$ star of solar metallicity, are shown in Figure 2, together with the electron mole number Ye and the integrated (from the surface of the star) abundances (in solar masses) of the two unstable nuclei. The three black solid vertical lines mark, left to right, the mass coordinates of the outermost layers where complete explosive Si burning (Six), incomplete explosive Si burning (Siix), and explosive O burning (Ox) occur. The dashed black vertical line marks the mass location corresponding to 0.07 $M_\odot$ of $^{56}$Ni ejected. $^{44}$Ti shows a major production in the Six region in presence of an $\alpha$-rich freeze-out (note the high final $\alpha$ abundance in this region), but it also shows the presence of two minor peaks, one in the region of the Siix and another in the region of Ox. $^{56}$Ni shows a composite production also, so that the relative abundance of these two nuclei depends on the region where they are synthesized. The cumulative abundance of both nuclei reflects these different behaviors. Moving toward the interior, both show a first steep rise due to the production by the Ox, then a shallower rise that reflects the contribution of the Siix, and eventually the final main rise due to the major contribution from the Six.

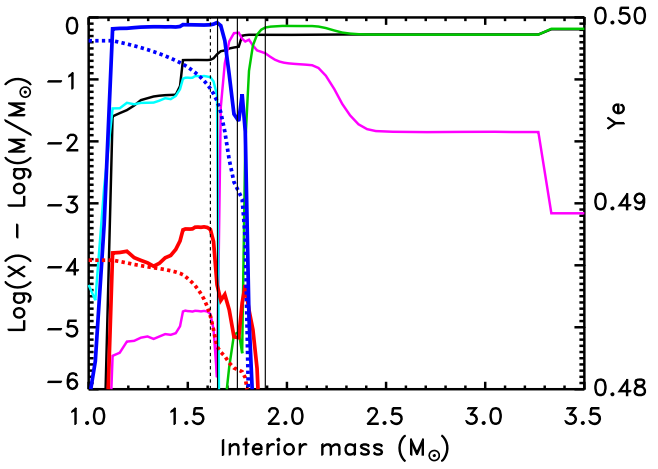


**Figure 2.** The distribution of $^{44}$Ti and $^{56}$Ni in a non-rotating 20 $M_\odot$ of solar metallicity after the passage of the shock wave. The various lines refer to O (green), Si (magenta), $\alpha$ (cyan), $^{44}$Ti (red), $^{56}$Ni (blue), Ye (black), integrated $^{44}$Ti (dashed red), and integrated $^{56}$Ni (dashed blue). All abundances are in mass fractions except for the two integrated abundances, which are in solar masses. The three solid black vertical lines mark, left to right, the borders of the Six, Siix, and Ox burning regions, while the dashed black vertical line marks the mass location corresponding to 0.07 $M_\odot$ of $^{56}$Ni ejected.

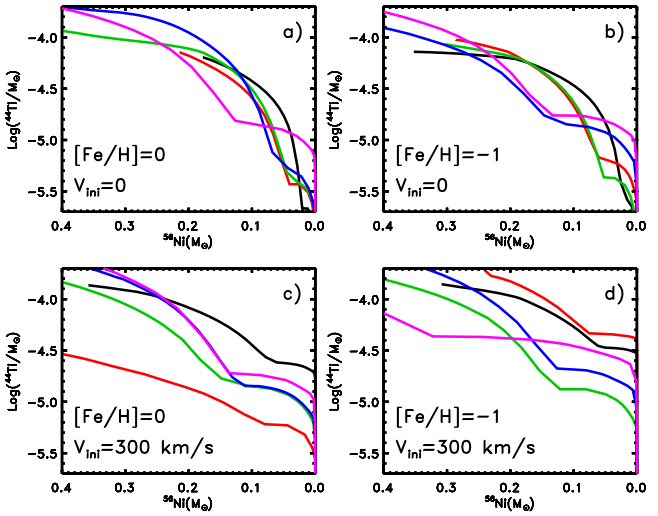


**Figure 3.** The trend of $^{44}$Ti vs. $^{56}$Ni for a sample of stars. The various lines refer to 13 $M_\odot$ (black), 15 $M_\odot$ (red), 20 $M_\odot$ (green), 25 $M_\odot$ (blue), and 40 $M_\odot$ (magenta). The (left) end point of each line corresponds to the maximum amount of $^{56}$Ni that may be ejected without simultaneously ejecting matter from the Fe core mass.

To visualize how the two cumulative abundances are connected to one another, Figure 3 shows a plot of $^{44}$Ti versus $^{56}$Ni for a subset of solar metallicity non-rotating models in panel (a). Each line refers to a stellar model and each point along a given line represents the amount of $^{44}$Ti that would be ejected together with the corresponding amount of $^{56}$Ni. Though the general trend is that the $^{44}$Ti ejected scales directly with $^{56}$Ni, it is possible to recognize in Figure 3 the different production zones identified in Figure 2. Each mass shows a first rise of $^{44}$Ti when the amount of $^{56}$Ni is still negligible (this component reflects the production by the Ox), then a shallow rise that corresponds to the contribution of the Siix, and the final steep rise that marks the contribution of the Six.

The first four columns of Table 1 show, for each metallicity and initial rotational velocity (and an assumed yield of 0.07 $M_\odot$ of $^{56}$Ni, a value close to the one determined for the SN 1987A) the following quantities: the initial mass, the mass cut, and the inner borders of the regions exposed, respectively, to the Siix and the Ox (all in solar masses). Columns 5–10 show the integrated abundances of the two unstable nuclei (again in solar masses) at the three mass coordinates given in columns 2–4, while the remaining columns show the respective percentage of production in the various zones. Note that, when the mass cut falls in the region of the Siix, the quantities reported in the columns marked as Siix and $M_{\rm cut}$ coincide.

The first thing worth noting is that the amount of $^{44}$Ti ejected by non-rotating models of solar metallicity ranges between 0.1 and 0.3 $\times$ $10^{-4}$ $M_\odot$ and falls short of the observed value of $\sim$1.3 $\times$ $10^{-4}$ $M_\odot$ (column 5 in the table) by at least a factor of four. Note that the mass cut falls within the Siix region in stars more massive than 25 $M_\odot$ (see columns 2 and 3): this means that these stars do not eject any matter exposed to the Six (columns 11 and 14) region where the maximum production of $^{44}$Ti occurs. Even in the range 15–25 $M_\odot$, a significant fraction of the 0.07 $M_\odot$ of $^{56}$Ni does *not* come from the Six region. In other words, since a large fraction of the required amount of $^{56}$Ni comes from layers more external to the region exposed to the Six, it is not possible to extract much matter from the Six zone where most of $^{44}$Ti is made; this explains why the yields of $^{44}$Ti are very low. However, even if it were possible to extract only matter exposed to Six (cancelling the contributions of the more external regions, i.e., the Six and the Ox), the amount of $^{44}$Ti that would correspond to 0.07 $M_\odot$ of $^{56}$Ni fully produced in the Six would not exceed $\sim$4 $\times$ $10^{-5}$ $M_\odot$. Panel (a) in Figure 3 clearly shows that an amount of $^{44}$Ti of the order of $10^{-4}$ $M_\odot$ would require the ejection of more than 0.2 $M_\odot$ of $^{56}$Ni, a value that is too large with respect to the value observed in the SN 1987A.

Lowering the metallicity does not help. Models computed for [Fe/H] $= -1$ do not vary significantly from the solar models (third panel in Table 1 and panel (b) in Figure 3) because both $^{44}$Ti and $^{56}$Ni are primary elements and therefore depend on the metallicity only indirectly through its influence on the evolutionary properties of a star (e.g., size of convective core, mass loss) but do not have a direct dependence on the initial metallicity (like secondary elements, e.g., N and the s-processes). At this metallicity, all stars more massive than 20 $M_\odot$ produce more than 0.07 $M_\odot$ of $^{56}$Ni outside the region of the Six and, hence, it is also difficult to extract material from the Six zone in this case (even an amount of the order of 0.10 $M_\odot$ of $^{56}$Ni would leave this discussion unaltered). Moving from [Fe/H] $= 0$ to [Fe/H] $= -1$, the yield of $^{44}$Ti reduces somewhat in the range 13 to 20 $M_\odot$, while the yield increases slightly in the more massive stars. Such a dependence must be considered with care because it largely depends on the adopted mass cut. Figure 4 shows (for both a 15 and a 40 $M_\odot$) a comparison of the $^{44}$Ti versus $^{56}$Ni relation between the two metallicities. The red lines refer to the 15 $M_\odot$ while the blue lines refer to the 40 $M_\odot$. The solid and dashed lines refer to [Fe/H] $= 0$ and [Fe/H] $= -1$, respectively. The figure clearly shows that the amount of $^{44}$Ti (as a function of the $^{56}$Ni ejected) produced by the Ox and the Siix (right side of the filled dots) increases as the metallicity decreases, while the opposite occurs within the region of Six (left side of the filled dots). There may actually be more than one intersection, due to the complex and non-monotonic interplay among the Ye profile, the mass–radius relation, and the passage of the shock wave. For the specific choice of 0.07 $M_\odot$ of $^{56}$Ni (solid black vertical

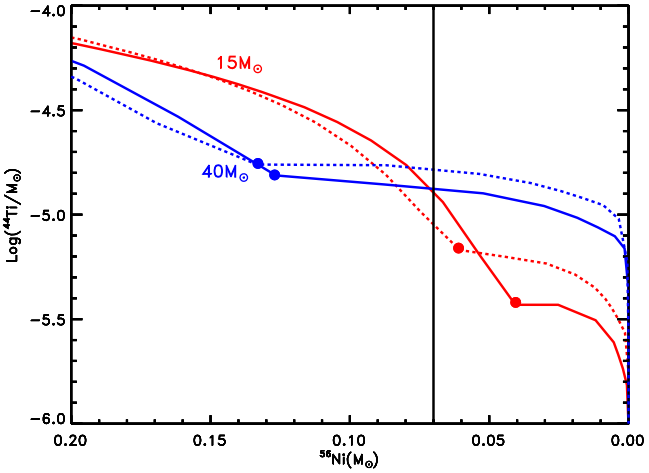


**Figure 4.** Comparison between the distribution of $^{44}$Ti vs. $^{56}$Ni in two stars of [Fe/H] = 0 (solid lines) and [Fe/H] = −1 (dashed lines). The red lines refer to a 15 $M_\odot$ while the blue lines to a 40 $M_\odot$. The filled dots mark the passage from the Six to the Siix. The solid black vertical line marks the mass location corresponding to 0.07 $M_\odot$ of $^{56}$Ni ejected.

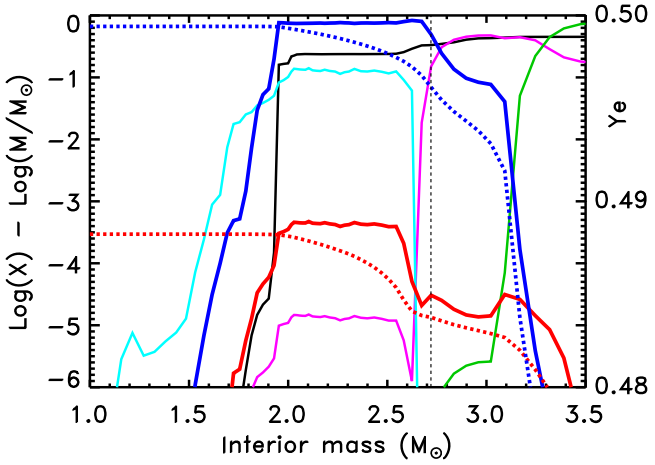


**Figure 5.** The distribution of $^{44}$Ti and $^{56}$Ni in a rotating 20 $M_\odot$ of solar metallicity after the passage of the shock wave. The various lines refer to O (green), Si (magenta), $\alpha$ (cyan), $^{44}$Ti (red), $^{56}$Ni (blue), Ye (black), integrated $^{44}$Ti (dashed red), and integrated $^{56}$Ni (dashed blue). The dashed black vertical line marks the mass location corresponding to 0.07 $M_\odot$ of $^{56}$Ni ejected.

line in Figure 4), the mass cut falls in the region of the Six for the mass range 13–20 $M_\odot$ and hence the $^{44}$Ti scales inversely with initial metallicity. Conversely, the more massive stars reach the chosen amount of $^{56}$Ni in the Siix and hence they show a direct scaling with the initial metallicity. What really matters, however, is that the dependence on the metallicity is in any case quite modest, remaining within a factor of two or so for the range of $^{56}$Ni of interest.

Summarizing the result obtained so far, analogously to what has been found for more than two decades by most authors working with 1D non-rotating models and spherically symmetric explosions, we cannot explain the $^{44}$Ti synthesized by the SN 1987A. The analysis of Cas A is much less stringent due to the lack of a good determination of the $^{56}$Ni ejected in that event (see Introduction).

Rotation basically leads to more massive He cores and to a lower amount of C at central He exhaustion (see Section 2). Hence it primarily affects the mass–radius relation at the onset of the collapse and the amount of mass that will be exposed to the various explosive burning. As an example, Figure 5 shows the structure of the rotating 20 $M_\odot$ of solar metallicity after the passage of the shock wave. The regions exposed to the various explosive burning are clearly much more extended in mass with respect to the non-rotating case (Figure 2), the Siix region, for example, extending over roughly one-half a solar mass, a factor of four or so bigger than in the non-rotating case. The second panel in Table 1 shows the data for the rotating solar metallicity models while panel (c) in Figure 3 shows the corresponding trend of $^{44}$Ti versus $^{56}$Ni. Rotating models at solar metallicity reach 0.07 $M_\odot$ of $^{56}$Ni in the Siix region in all models more massive than 15 $M_\odot$. As a consequence the yields of $^{44}$Ti synthesized by rotating models are, in most cases, *even lower* than those of the non-rotating ones. Note, however, that the amount of $^{44}$Ti produced by the Ox increases in rotating models because the thickness of the region exposed to this burning increases.

Rotating models at [Fe/H] = −1 (summarized in the fourth panel in Table 1 and panel (d) in Figure 3) show a qualitatively similar behavior, the rotating stars reaching 0.07 $M_\odot$ of $^{56}$Ni again well within the Siix region in all models more massive than 15 $M_\odot$. This time, however, the amount of $^{44}$Ti produced

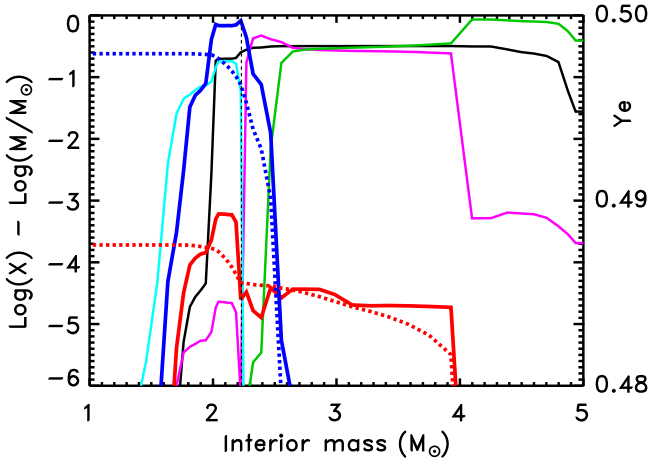


**Figure 6.** The distribution of $^{44}$Ti and $^{56}$Ni in a rotating 15 $M_\odot$ of [Fe/H] = −1 after the passage of the shock wave. The various lines refer to O (green), Si (magenta), $\alpha$ (cyan), $^{44}$Ti (red), $^{56}$Ni (blue), Ye (black), integrated $^{44}$Ti (dashed red), and integrated $^{56}$Ni (dashed blue). The dashed black vertical line marks the mass location corresponding to 0.07 $M_\odot$ of $^{56}$Ni ejected.

is larger than in the non-rotating case because of a more consistent contribution of the Siix and Ox to its synthesis. But low metallicity rotating models show a very interesting feature in the two lowest masses, 13 and 15 $M_\odot$, i.e., the formation of a wide O convective shell that extends over more than 1.5 $M_\odot$. The O burning shell is always a nursery of $^{44}$Ti (this occurrence was already noted by Tur et al. (2010)), but this layer is always so close to the mass cut that it is completely swept out by the shock wave. The formation of a very extended O convective shell, on the contrary, preserves most of this $^{44}$Ti because convection pushes the freshly made $^{44}$Ti at a large distance where it is not affected by the passage of the blast wave. Figure 6 shows the distribution of the nuclei relevant for the present discussion in a rotating 15 $M_\odot$ having [Fe/H] = −1 and, in particular, the large amount of $^{44}$Ti produced by the O burning shell spread over the wide convective region and left almost untouched by the shock wave. The formation of unusually extended convective shells is not so rare. Zero metallicity stars, for example, often experience such an

occurrence due to the low entropy barrier between the He- and H-rich zones. We have already shown, in Limongi & Chieffi (2006), that the extension of convective zones significantly affects the yields of other nuclear species, such as $^{26}$Al and $^{60}$Fe. Let us also note that the current description of convection in general, but in particular in the more advanced phases, may be very different from what we model in 1D: according to the studies of, e.g., Meakin & Arnett (2007) and Arnett et al. (2009), the O convective shell could develop through flames that could extend very far from the burning location. This result could account for the different behavior between the average stars, which do not produce a large amount of $^{44}$Ti, and some specific cases in which rotation may lead to the formation of an extended convective shell where a much larger amount of $^{44}$Ti may be synthesized and preserved.

Another important constraint that cannot be neglected in the analysis of the combined synthesis of $^{44}$Ti and $^{56}$Ni is the ratio $^{44}$Ca/$^{56}$Fe in the solar chemical composition. According to Asplund et al. (2009), this ratio (by number) in the Sun is $1.57 \times 10^{-3}$. By assuming that all solar metallicity stars between 13 and 120 $M_{\odot}$ eject 0.07 $M_{\odot}$ of $^{56}$Ni and integrating over a Salpeter IMF ($x = 1.35$) we get a ratio of $^{44}$Ca/$^{56}$Fe $= 7.1 \times 10^{-4}$ in the non-rotating case and equal to $1.1 \times 10^{-3}$ for rotating models. In such a scenario, the ejecta of stars more massive that 25 $M_{\odot}$ must have a final kinetic energy in excess of $3 \times 10^{51}$ erg in order to eject even a minor fraction of $^{56}$Ni, and this amount is incompatible with the average kinetic energy of a sample of core collapse supernovae (Pejcha & Prieto 2015; Lyman et al. 2016); if one would set the maximum kinetic energy of the ejecta to $3 \times 10^{51}$ erg, all stars more massive that 25 $M_{\odot}$ fail to explode and collapse completely, contributing to the chemical enrichment only through the wind. Note also that the works of O'Connor & Ott (2011) and Sukhbold et al. (2016) support this idea: O'Connor & Ott (2011) define, on the basis of a large set of hydro simulations, a compactness parameter $\xi$ that allows them to "predict" the final fate of a collapsing star. They find that a value of $\xi$ of the order of 0.45 marks the transition from structures that collapse to a black hole to those that do not. All of our models of mass larger than 25 $M_{\odot}$ have a compactness parameter $\xi$ well above 0.45. Sukhbold et al. (2016) followed the explosions of a very fine grid of models in the range 9–120 $M_{\odot}$ and found a complex, non-continuous distribution of models that explode and those that do not explode. However most of their models having initial mass larger than 28 $M_{\odot}$ or so fully collapse without exploding. In a scenario in which stars more massive than 25 $M_{\odot}$ fail to explode, our models would predict these ratios (by number) for $^{44}$Ca/$^{56}$Fe: $1 \times 10^{-3}$([Fe/H] $= 0$, $v = 0$) and $1.4 \times 10^{-3}$([Fe/H] $= 0$, $v = 300$ km s$^{-1}$). Given the many uncertainties in the modeling of both the hydrostatic evolution as well as the explosion of a stellar model, we think that the present set of models predicts a ratio compatible with the observed value, in particular for the second scenario in which all stars more massive than 25 $M_{\odot}$ are assumed to completely collapse without any ejecta apart from the mass lost through the wind.

All of these results imply that the amount of $^{44}$Ti and $^{56}$Ni predicted by our models can account for the $^{44}$Ca/$^{56}$Fe ratio in the solar chemical composition without the necessity of additional $^{44}$Ti from the majority of the stars. This result also agrees with the fact that, if any massive star would eject an amount of $^{44}$Ti of the order of $(1.3 \div 1.5) \times 10^{-4}$ $M_{\odot}$, the current all-sky maps should have detected a clear signal from, e.g., the galactic center, which has not been observed (Tsygankov et al. 2016).

SN 1987A and possibly Cas A could be rarer events in which the formation of an extended O convective shell (due to rotation and/or a more reliable description of the thermal instabilities) could contribute to the synthesis of $^{44}$Ti. A (partial) decoupling of the region where $^{44}$Ti and $^{56}$Ni are synthesized could also help in the understanding of the lack of correlation between the $^{44}$Ti and the Fe X-ray emission in Cas A (Grefenstette et al. 2014).

This research has been partially supported by the agreement ASI/INAF No. 2013-025.R1 and by the National Institute for Astrophysics (INAF) through the grant PRIN-2014 (Transient Universe, unveiling new types of stellar explosions with PESSTO).

## References

Ahmad, I., Greene, J. P., Moore, E. F., et al. 2006, PhRvC, 74, 065803
Arnett, D., Meakin, C., & Young, P. A. 2009, ApJ, 690, 1715
Asplund, M., Grevesse, N., Sauval, A. J., & Scott, P. 2009, ARA&A, 47, 481
Bodansky, D., Clayton, D. D., & Fowler, W. A. 1968, ApJS, 16, 299
Boggs, S. E., Harrison, F. A., Miyasaka, H., et al. 2015, Sci, 348, 670
Catchpole, R. M., Whitelock, P. A., Feast, M. W., et al. 1988, MNRAS, 231, 75
Cayrel, R., Depagne, E., Spite, M., et al. 2004, A&A, 416, 1117
Chieffi, A., & Limongi, M. 2013, ApJ, 764, 21
Colella, P., & Woodward, P. R. 1984, JCoPh, 54, 174
Dupraz, C., Bloemen, H., Bennett, K., et al. 1997, A&A, 324, 683
Eriksen, K. A., Arnett, D., McCarthy, D. W., & Young, P. 2009, ApJ, 697, 29
Grebenev, S. A., Lutovinov, A. A., Tsygankov, S. S., & Winkler, C. 2012, Natur, 490, 373
Grefenstette, B. W., Harrison, F. A., Boggs, S. E., et al. 2014, Natur, 506, 339
Iyudin, A. F., Diehl, R., Bloemen, H., et al. 1994, A&A, 284, L1
Leising, M. D., & Share, G. H. 1994, ApJ, 424, 200
Limongi, M., & Chieffi, A. 2003, ApJ, 592, 404
Limongi, M., & Chieffi, A. 2006, ApJ, 647, 483
Lyman, J. D., Bersier, D., James, P. A., et al. 2016, MNRAS, 457, 328
Maeda, K., & Nomoto, K. 2003, ApJ, 598, 1163
Magkotsios, G., Timmes, F. X., Hungerford, A. L., et al. 2010, ApJS, 191, 66
Mahoney, W. A., Ling, J. C., Wheaton, W. A., & Higdon, J. C. 1992, ApJ, 387, 314
Meakin, C. A., & Arnett, D. 2007, ApJ, 665, 690
O'Connor, E., & Ott, C. D. 2011, ApJ, 730, 70
Pejcha, O., & Prieto, J. L. 2015, ApJ, 806, 225
Rauscher, T., Heger, A., Hoffman, R. D., & Woosley, S. E. 2002, ApJ, 576, 323
Seitenzahl, I. R., Timmes, F. X., & Magkotsios, G. 2014, ApJ, 792, 10
Siegert, T., Diehl, R., Krause, M. G. H., & Greiner, J. 2015, A&A, 579, A124
Spite, M., Cayrel, R., Plez, B., et al. 2005, A&A, 430, 655
Sukhbold, T., Ertl, T., Woosley, S. E., Brown, J. M., & Janka, H.-T. 2016, ApJ, 821, 38
The, L.-S., Clayton, D. D., Diehl, R., et al. 2006, A&A, 450, 1037
The, L.-S., Clayton, D. D., Jin, L., & Meyer, B. S. 1998, ApJ, 504, 500
Thielemann, F.-K., Nomoto, K., & Hashimoto, M.-A. 1996, ApJ, 460, 408
Tsygankov, S. S., Krivonos, R. A., Lutovinov, A. A., et al. 2016, MNRAS, 458, 3411
Tur, C., Heger, A., & Austin, S. M. 2010, ApJ, 718, 357
Woosley, S. E., Arnett, W. D., & Clayton, D. D. 1973, ApJS, 26, 231
Woosley, S. E., & Weaver, T. A. 1995, ApJS, 101, 181